Sensors and Materials, Vol. 37, No. 5 (2025) 1809–1823
MYU Tokyo

S & M 4019

Integrating Cellulose Nanocrystals, Antimicrobial Photodynamic Inactivation, and Poly[2-(tert-butylamino)ethyl methacrylate] into a 3D-printed Multifaceted Antimicrobial Sensor Material for Enhanced Sterilization and Wound Care Applications

Shih-Chen Shi,[1*] Yu-Chen Xu,[1] Chih-Kuang Chen,[2]
Dieter Rahmadiawan,[1,3] and Bao-Tsan Ko[4]

[1]Department of Mechanical Engineering, National Cheng Kung University (NCKU),
No. 1, University Road, Tainan 70101, Taiwan
[2]Department of Materials and Optoelectronic Science, National Sun Yat-sen University, Kaohsiung 80424, Taiwan
[3]Department of Mechanical Engineering, Universitas Negeri Padang, 25173 Padang, Sumatera Barat, Indonesia
[4]Department of Chemistry, National Chung-Hsing University, Taichung 402, Taiwan

(Received August 16, 2024; accepted November 28, 2024)

Keywords: cellulose nanocrystals, antimicrobial photodynamic inactivation, poly[2-(tert-butylamino) ethyl methacrylate], 3D printing, sensors

The development of sensor materials with antimicrobial properties is crucial for advancing biomedical applications, particularly in sterilization and wound care. In this study, we present a novel approach to fabricating a multifunctional sensor material by integrating cellulose nanocrystals (CNCs) with antimicrobial photodynamic inactivation (aPDI) and poly[2-(tert-butylamino)ethyl methacrylate] (PTA) within a 3D-printed composite. CNCs, known for their biocompatibility and functional surface chemistry, serve as an ideal platform for embedding antimicrobial agents. Erythrosine, a photosensitizer, is used to activate aPDI, whereas PTA provides additional antimicrobial efficacy. The sensor material's antimicrobial performance was evaluated, demonstrating the complete inactivation of *Escherichia coli* and *Staphylococcus aureus* under green and white light irradiations. The integration of CNCs with aPDI and PTA enhances the material's sensing capabilities, allowing for the real-time monitoring of microbial contamination. This composite material is a promising candidate for applications in wound care and sterilization, providing both structural support and antimicrobial functionality.

1. Introduction

In the evolving field of sensor technology, particularly for biomedical applications, there is a pressing need for materials that not only detect environmental changes but also offer antimicrobial properties to address bacterial contamination. The increase in antimicrobial resistance underscores the importance of developing advanced materials that combine sensing capabilities with effective microbial inactivation.[1,2] The prevalence of bacterial resistance to

*Corresponding author: e-mail: scshi@mail.ncku.edu.tw
https://doi.org/10.18494/SAM5312

ISSN 0914-4935
https://myukk.org/

conventional antimicrobial agents has underscored the necessity for innovative approaches that circumvent the mechanisms through which bacteria develop resistance.[3] Additionally, there is a growing recognition of the impact that sterilization techniques can have on the integrity and performance of polymer-based medical devices, highlighting the need for sterilization methods that preserve material properties while effectively eliminating microbial contaminants.[4]

Among the innovative strategies for creating such materials, antimicrobial photodynamic inactivation (aPDI) has emerged as a powerful tool. aPDI involves the use of light-activated photosensitizers that, upon irradiation with specific wavelengths of light, produce reactive oxygen species (ROS) capable of inactivating a broad spectrum of microbes.[5] This approach offers the significant advantage of not promoting bacterial resistance, a critical concern in the current era of increasing antimicrobial resistance.[6] Furthermore, the development of antimicrobial polymers, such as poly[2-(tert-butylamino)ethyl methacrylate] (PTA), represents a parallel avenue of research.[7] PTA and similar polymers offer antimicrobial efficacy coupled with low toxicity toward human cells and tissues, addressing the challenge of balancing antimicrobial potency with biocompatibility.[8]

Research on nontoxic or natural-based materials for biomedical applications has been extensive in this decade.[9–13] Cellulose, the most abundant polymer on earth, stands at the forefront of innovative antimicrobial strategies in contemporary biomedical research.[14] Its outstanding mechanical properties, inherent biocompatibility, and facile functionalization render it an exceptional candidate for biomedical applications.[15] Among the various cellulose derivatives, cellulose nanocrystals (CNCs) emerge as the most promising for antimicrobial purposes owing to their unique physicochemical attributes.[16,17]

CNCs boast a high surface area-to-volume ratio, significantly enhancing their interaction with microbial entities. Moreover, the abundance of reactive hydroxyl groups on their surfaces presents a versatile platform for the attachment of diverse functional molecules.[18] This feature is particularly advantageous for the conjugation of photosensitizers utilized in aPDI and the integration of antimicrobial polymers such as PTA. The combination of CNCs' structural and chemical properties with these antimicrobial agents positions CNCs as a cornerstone in the development of advanced materials designed to effectively combat microbial infections.

Combining CNCs with antimicrobial strategies such as aPDI and PTA is expected to create a composite material with superior antimicrobial properties.[19] The controlled release capabilities of CNCs, paired with the broad-spectrum microbial inactivation of aPDI, suggest that the resulting material can provide a comprehensive approach to antimicrobial intervention. Such a material is not only relevant for the treatment of chronic wounds and infections but also for the sterilization of medical devices, where traditional methods may compromise the material integrity or contribute to the development of drug resistance.

The advent of polymer 3D printing technology has opened new horizons for the application of these antimicrobial materials in medical research and device fabrication.[20,21] 3D printing offers the unparalleled ability to create complex, patient-specific geometries, such as meniscal implants, that closely mimic the structure and function of native tissues.[22] The incorporation of CNC-based antimicrobial materials into 3D-printed devices can significantly enhance their

therapeutic potential, offering both structural support and localized antimicrobial activity to prevent infection.

In this study, we explore the integration of CNCs with aPDI and PTA into a 3D-printed sensor material. The resulting composite not only enhances antimicrobial performance but also provides a platform for monitoring microbial presence, bridging the gap between material science and sensor technology.

2. Materials and Methods

2.1 Sample preparation

The CNC–g–PTA was prepared as follows: about 1 g of CNCs was added to water to prepare a 10 wt% CNC/H_2O solution. Reagent-grade acetone (450 mL) was added to the CNC/H_2O solution, and the mixture was stirred overnight. After removing the supernatant, the precipitate was redispersed in 40 mL of acetone, mixed thoroughly three times, and then centrifuged. Next, dimethylformamide (DMF) (50 mL) was added, and the mixture was poured into a round-bottom flask after thorough mixing. 4 g of 4-dimethylaminopyridine and 8 mL of triethylamine were added sequentially, and the resulting mixture was stirred for 30 min. Subsequently, after placing the mixture in an ice bath, 8 mL of 2-bromoisobutyryl bromide (BiBB) was added dropwise. The ice bath was then removed 15 min after the completion of the dropwise addition, and the reaction was allowed to proceed for 48 h. After the completion of the reaction, the resultant CNC–Br was sequentially washed by centrifugation using ethanol, tetrahydrofuran (THF), and a mixture of acetone and water and then dried in a 50 °C oven for one day to obtain the final CNC–Br product. The resultant CNC–Br (50 mg) was mixed with DMF (80 mL). Subsequently, 14.68 μL of α-bromoisobutyryl bromide, 30 mL of the 2-(tert-butylamino)ethyl methacrylate (TA) monomer, and 108.8 μL of 1,1,4,7,10,10-hexamethyltriethylenetetramine were sequentially added to the reaction flask. The solution in the reaction flask was then frozen, vacuumed, and thawed three times. After freezing for the fourth time, CuBr was added, and the solution was vacuumed for 1 h, followed by thawing, and subjected to a final round of freezing, vacuuming, and thawing. The resulting solution was allowed to react for 48 h. After the completion of the reaction, the product was washed three times by stirring and centrifuging with THF, ethanol, and water, in order to remove residual free polymers and unreacted chemical substances. The washed product was then placed in pure water, subjected to dialysis for two days, and then dried in an oven to obtain the CNC–g–PTA.

The obtained CNC–g–PTA (1 g) was used to prepare a 1 wt% suspension and 6 g of $NaIO_4$ was added to the suspension under pH 4.5 and 45 °C reaction conditions, and the mixture was stirred for 12 h. After the completion of the reaction, the reaction product was subjected to dialysis for four days and freeze-dried to obtain the aldehyde-functionalized dialdehyde CNC (DACNC)–g–PTA. Subsequently, 100 mg of erythrosine was added to 100 ml of 1 wt% suspension of DACNC–g–PTA; the mixture of the two materials was then mixed in an ultrasound bath to prepare the erythrosine (Ery)–DACNC–g–PTA.

2.2 Microbial inactivation testing

Microbial inactivation testing was performed in two stages using Ery–DACNC–g–PTA and 3D-printed silicone/Ery–DACNC–g–PTA. For 3D printing, the sample was mixed with silicone by ultrasonication to ensure an even dispersion. The resulting mixture was loaded into a 3D printer, and the printer settings were adjusted according to the silicone specifications. The 3D structures were printed and then cured as per the manufacturer's instructions, which could involve room temperature curing or heating. Once cured, the 3D-printed objects were removed from the print bed and checked for defects and an even distribution of Ery–DACNC–g–PTA.

2.2.1 aPDI test

Green and white LED lights were used as light sources. *E. coli* and *S. aureus* cultures were diluted to an optical density (OD) of ~ 0.1 at a wavelength of 600 nm for use as experimental bacterial solutions. A 1.5 wt% Ery–DACNC–g–PTA suspension was prepared. 400 μL of the solution was mixed thoroughly with 1 mL of the bacterial suspension. The inactivation degrees of *E. coli* and *S. aureus* were measured after 30 and 60 min of green and white light irradiations, respectively. The experiments were performed in triplicate for each group.

2.2.2 Light-free microbial inactivation

About 400 μL of a 1.5 wt% Ery–DACNC–g–PTA suspension was mixed with 1 mL of the bacterial suspension. The bacterial suspension was diluted to an OD value of 0.1 at a wavelength of 600 nm and cultured for 1 d in the dark environment. The inactivation degrees of *E. coli* and *S. aureus* were measured separately by light-free microbial inactivation, and the experiments were performed in triplicate for each group.

2.2.3 Reusability of the aPDI effect

A 1.5 wt% Ery–DACNC–g–PTA suspension was prepared. 400 μL of the composite suspension was then transferred to a sample vial. Subsequently, 1 mL of the diluted bacterial suspension was added and then thoroughly mixed. Composite suspensions with and without an added bacterial suspension were irradiated using a 7.2 W green LED light source for 30 min. The bacterial viability in the sample vials with the added bacterial suspension was measured by the colony-forming unit (CFU) plate count method, and the microbial inactivation degree was calculated. The composite suspension without the added bacterial solution was freeze-dried to obtain a composite material that had undergone one round of aPDI. After 96 h of freeze drying, the material was subjected to a second round of aPDI using the same process, and the microbial inactivation degree was recalculated. This experimental process was performed in triplicate or terminated when the microbial inactivation degree reached > 90%. The experiment was conducted using three samples from each group, and the inactivations of *E. coli* and *S. aureus* were tested separately.

2.3 3D printing of human meniscal cartilage

The Ery–DACNC–g–PTA was thoroughly mixed with silicone A in a 1:9 mass ratio to obtain resin A for 3D printing. Resin B was prepared as previously described in Sect. 2.2. A sketch of the meniscus was created in SolidWorks, saved as an STL file, and imported into FAMufacture software (San Draw, Taiwan) to print the final product using a 3D printer.

2.3.1 Mechanical properties

A tensile specimen with a cross-sectional area of 3 × 3 mm^2 and a length of 15 mm was designed in SolidWorks and printed using the 3D printer. The tensile strengths of the specimens were tested using a precision universal tensile testing machine (AGS-X, SHIMADZU, Japan).

2.3.2 Antimicrobial capability of meniscal implants

Using the 3D printer, we printed the test specimens with a length of 1 cm, a width of 1 cm, and a thickness of 1 cm. An *E. coli* solution with an OD value of 0.1 was prepared. The printed test specimens were placed in sample vials, and 1 mL of the prepared bacterial solution was added to each sample vial. The microbial inactivation degrees were measured separately after 30 min of green light irradiation, 60 min of white light irradiation, and one day of culture without light. The experiments were performed in triplicate for each group. Each experiment was repeated using an *S. aureus* bacterial suspension to determine the inactivation effects against *S. aureus*.

2.3.3 Duration of effective microbial inactivation by meniscal cartilage

Before the meniscus implants were implanted in the human body, to maintain a sterile state, the bacteria on the surface of the meniscus implants were removed by PDI treatment. In addition, after being implanted into the human body, the sterile effect of the surface of the meniscus implants was permanently maintained by PTA contact sterilization. The following process was used to determine the duration of the PDI treatment of the meniscal implants. During weeks 4 and 7, the PDI treatment was performed using silicone samples containing the antimicrobial material. The inactivations of *E. coli* and *S. aureus* after 30 min of green light irradiation were measured to determine the material's service life.

2.3.4 Biocompatibility testing

Cytotoxicity was analyzed according to the ISO 10993-5 standard test method. A 3D-printed test specimen was placed in Dulbecco's Modified Eagle's medium (DMEM) to form a suspension at a concentration of 5 mg/mL and subsequently cultured at 37 °C for 24 h. The suspension was centrifuged after 24 h of culture, and the supernatant was used as the stock suspension. The resultant stock solution was diluted using DMEM. On the basis of the dilution

ratios, the concentrations of the extract solutions were determined to be 10, 25, 50, 75, and 100% (by volume percentage). After preparing the extract solutions, L929 cells were seeded in a 96-well plate at a density of 5×10^3 cells/well. After culturing for 24 h, the culture medium was replaced with the extract suspension at the above-mentioned five different concentrations. After 24 and 48 h of culture, the extract solution used for coculturing was removed from the wells. Each well was washed with fresh PBS (pH 7.4), and then added with 100 μL of MTT solution (5 mg/mL in DMEM). The 96-well plate was allowed to stand in a 37 °C/ 5% CO_2 environment for 4 h. Subsequently, the culture medium in the wells was removed, and the resultant formazan product was dissolved in 100 μL of dimethyl sulfoxide. The 96-well plate was subsequently placed in an incubator for 5 min to react with the well contents. After incubation, the OD of the solution in each well was measured at a wavelength of 450 nm using a microplate reader (Multiskan, Thermo Fisher Scientific, USA). The OD of the untreated L929 cells was used as a reference (100%), and the results of the cell viability testing were expressed as percentages of the OD of untreated cells.

3. Results and Discussion

3.1 Chemical structure of Ery–DACNC–g–PTA

Figure 1 shows the Fourier transform infrared spectroscopy (FTIR) spectra of CNCs, CNC–Br, and CNC–g–PTA. Compared with the CNCs, CNC–Br exhibited an additional characteristic peak of C=O at 1722 cm^{-1}, which demonstrated the successful grafting of BiBB onto the surface of the CNCs. The broad stretching band of –OH groups at 3600–3100 cm^{-1} was also reduced, indicating that certain –OH groups were replaced and converted into ester

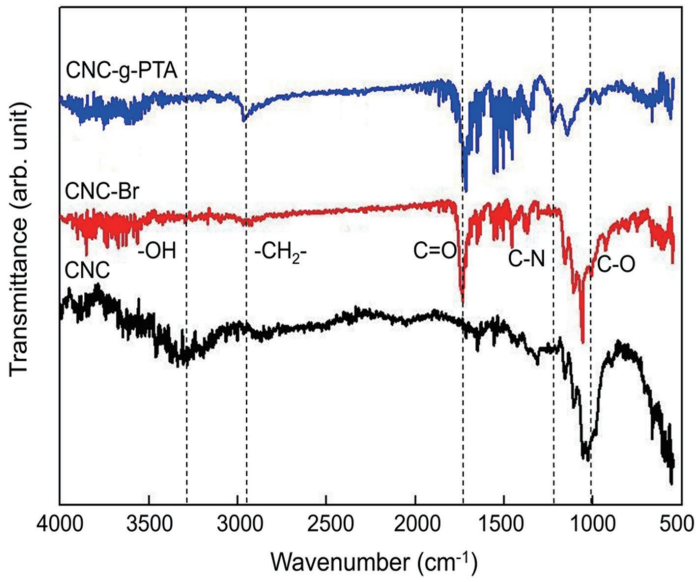

Fig. 1. (Color online) FTIR spectra of CNCs, CNC–Br, and CNC–g–PTA.

bonds.[23] Compared with the two spectra mentioned above, the spectrum of CNC–g–PTA showed a peak at 2962 cm^{-1}, attributed to the asymmetric stretching vibrations of $–CH_2–$ in the main chain of PTA.[24] A peak corresponding to the stretching vibration of C=O was also observed at 1722 cm^{-1}. The characteristic peaks corresponding to C–N and C–O were observed at 1233 and 1054 cm^{-1}, respectively.

Figure 2 shows the FTIR spectra of CNC–g–PTA, DACNC–g–PTA, and Ery–DACNC–g–PTA composites. Compared with CNC–g–PTA, DACNC–g–PTA showed a characteristic peak corresponding to the aldehyde group (C=O) at around 1735 cm^{-1}, indicating a successful aldehyde functionalization.[25] A smaller number of –OH groups were converted into C=O after aldehyde functionalization, apparent from the weakening of the characteristic peak signal of the –OH groups in the range of 3000–3500 cm^{-1}.[26]

After adding erythrosine, the characteristic peak of C=O at around 1735 cm^{-1} was weakened, and a characteristic peak of carboxylates appeared at ~ 1550 cm^{-1}, indicating that erythrosine was grafted onto the DACNC–g–PTA through the aldehyde groups. The enhancement of the aromatic ring (C=C) signal at ~ 1450 cm^{-1} and the presence of an ether (R–O–R) signal at ~ 1240 cm^{-1} provided further evidence of the excellent performance of DACNC–g–PTA and erythrosine combination.

3.2 Microbial inactivation capability of Ery–DACNC–g–PTA

3.2.1 Microbial inactivation testing

Figures 3 and 4 show the CFU plate counts for the control groups, the mixtures of a bacterial solution, and the composite material for *E. coli* and *S. aureus*. Each control group was established by adding 1 mL of the bacterial solution to a sample vial without any treatment, followed by 1 d

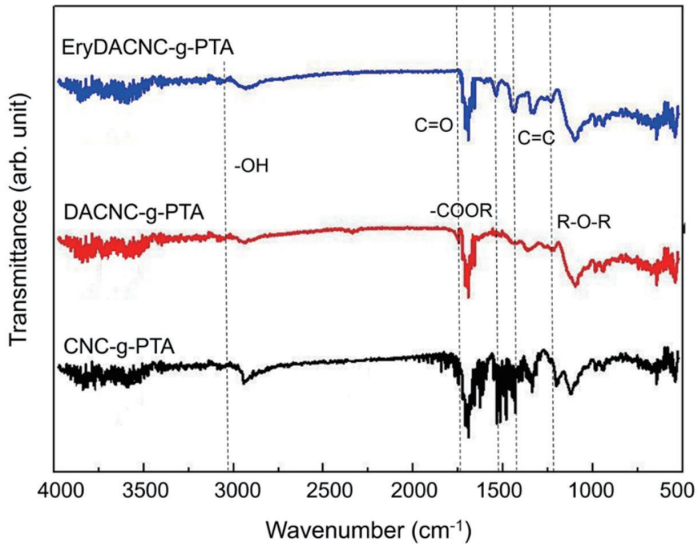

Fig. 2. (Color online) FTIR spectra of CNC–g–PTA, DACNC–g–PTA, and Ery–DACNC–g–PTA composites.

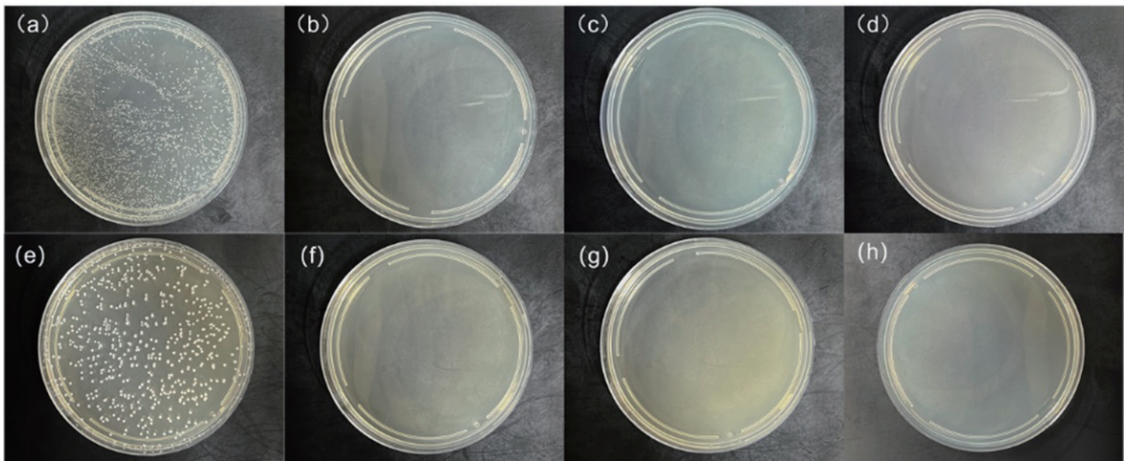

Fig. 3. (Color online) Growth of *E. coli* (a) in the control group, (b) after 30 min of green light irradiation, (c) after 60 min of white light irradiation, and (d) in the absence of light. Growth of *S. aureus* (e) in the control group, (f) after 30 min of green light irradiation, (g) after 60 min of white light irradiation, and (h) in the absence of light.

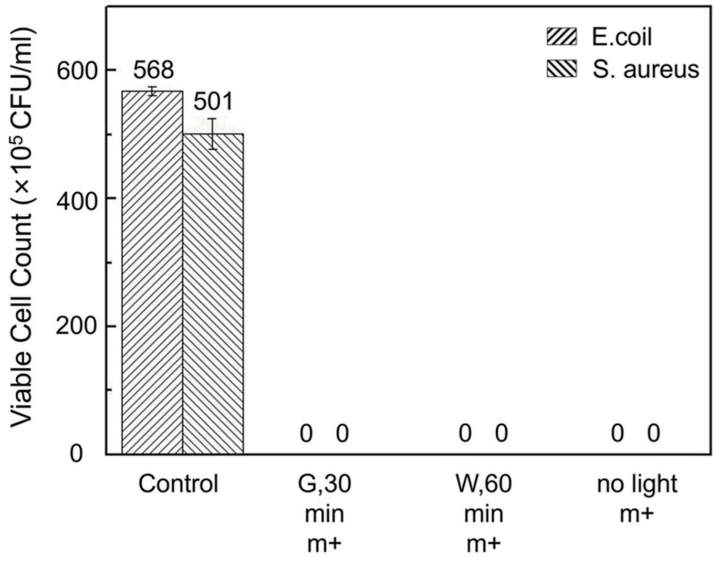

Fig. 4. Inactivation effects on *E. coli* and *S. aureus* under different conditions. G: green LED light irradiation; W: white LED light irradiation; 0: complete inactivation; m+: with Ery–DACNC–g–PTA.

of culture in an incubator. In Fig. 4, zero denotes the absence of detectable bacteria. Ery–DACNC–g–PTA completely inactivated *E. coli* after 30 min of green light irradiation and 60 min of white light irradiation. In the absence of light, Ery–DACNC–g–PTA completely inactivated *E. coli* after 1 d of mixed culture. Similarly, Ery–DACNC–g–PTA completely inactivated *S. aureus* after 30 min of green light irradiation, 60 min of white light irradiation, and 1 d of mixed culture without light.

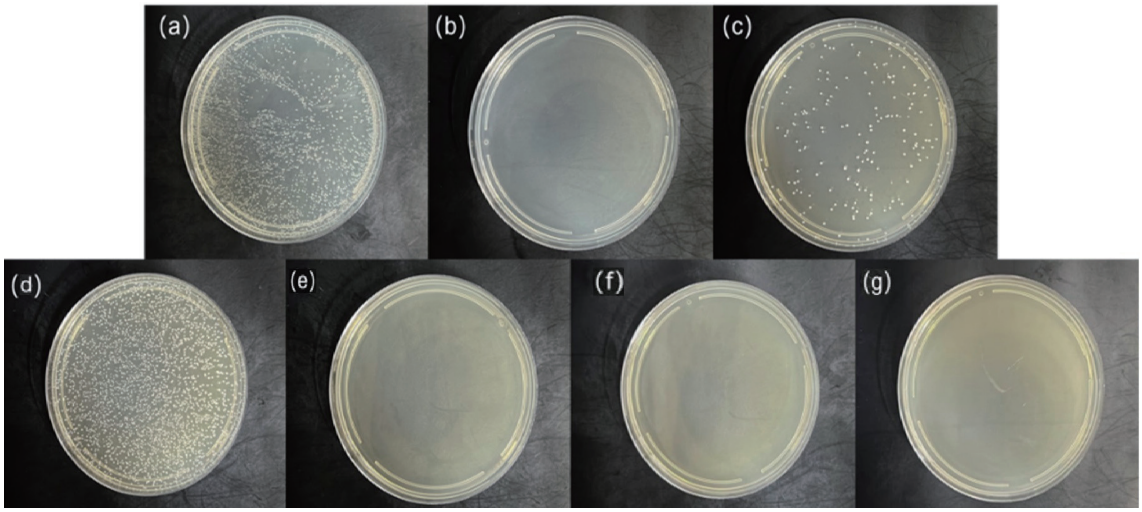

Fig. 5. (Color online) Viability of *E. coli* (a) in the control group, (b) after the first round of PDI treatment, and (c) after the second round of PDI treatment. Viability of *S. aureus* (d) in the control group, (e) after the first round of PDI treatment, (f) after the second round of PDI treatment, and (g) after the third round of PDI treatment.

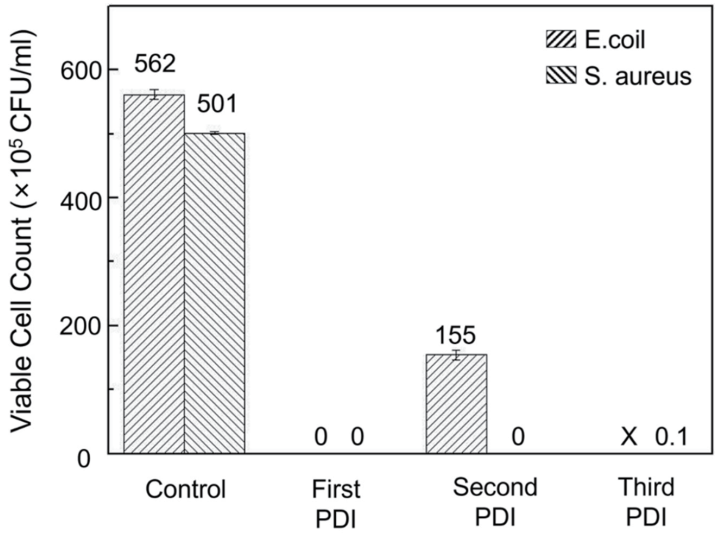

Fig. 6. Inactivation effects of different rounds of PDI treatment on *E. coli* and *S. aureus.* 0: complete inactivation; X: third round of PDI treatment was not performed on *E. coli*.

3.2.2. Reusability of aPDI effect

Figures 5 and 6 show the results of the repeated aPDI of *E. coli* and *S. aureus*. The control group was established by adding 1 mL of the bacterial solution to a sample vial without any treatment, followed by one day of culture in an incubator. Reusability was tested by subjecting the composite material to multiple rounds of aPDI. The material maintained a high degree of bacterial inactivation, particularly against *S. aureus*, even after multiple rounds of treatment.

Although the inactivation degree of *E. coli* decreased to 72% after the second round of green light irradiation for 30 min, the expected level of inactivation was not reached. However, *S. aureus* was inactivated entirely by the second round of aPDI, and the inactivation degree remained above 99.9%, even during the third round.

3.3 Properties of 3D-printed human meniscal cartilage

3.3.1 Mechanical properties

Table 1 lists the tensile strengths of the 3D-printed test specimens obtained after mixing the antimicrobial material and silicone in a 1:9 mass ratio. When an infill density of 95% was used as the printing parameter, the tensile strength of the resultant test specimen was 13.3 MPa, which is within the tensile strength range of the human meniscus. Therefore, the value of 95% was adopted as the parameter value for the 3D printing of the human meniscus model.

3.3.2 Microbial inactivation by 3D-printed meniscal implant

Figures 7 and 8 show the viable CFU counts of *E. coli* and *S. aureus* in various groups. The control group was established by adding 1 mL of the bacterial suspension to a sample vial

Table 1
Mechanical properties of 3D-printed meniscus using 10 wt% of antimicrobial material under different infill densities. Infill density refers to the percentage of the internal structure filled with material during 3D printing.

Parameter	Tensile strength (MPa)	Maximum strain (%)
Human meniscus	11.7 ± 2.1[36]	–
95% infill density	13.3	594
100% infill density	14.8	603

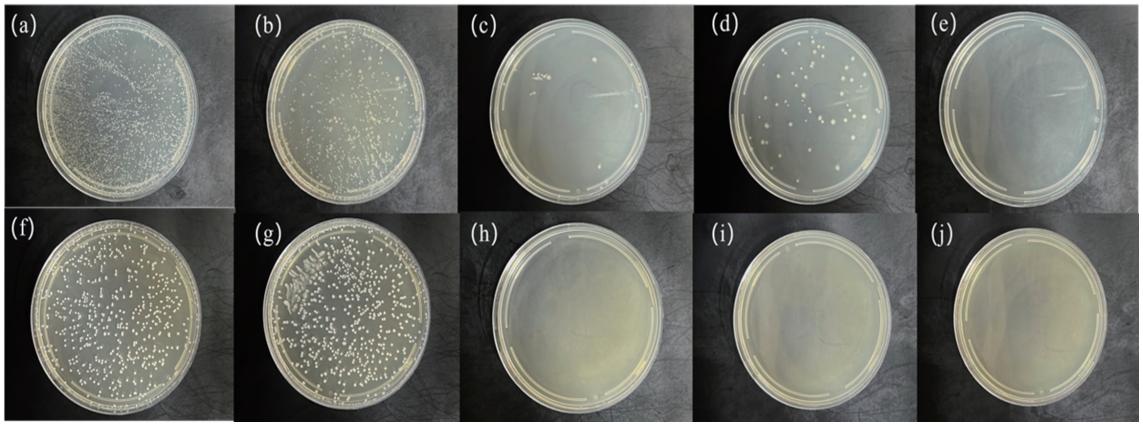

Fig. 7. (Color online) Growth of *E. coli* (a) in the control group, (b) when cultured with a pure silicone test specimen, (c) after 30 min of green light irradiation, (d) after 60 min of white light irradiation, and (e) in the absence of light. Growth of *S. aureus* (f) in the control group, (g) when cultured with a pure silicone test specimen, (h) after 30 min of green light irradiation, (i) after 60 min of white light irradiation, and (j) in the absence of light.

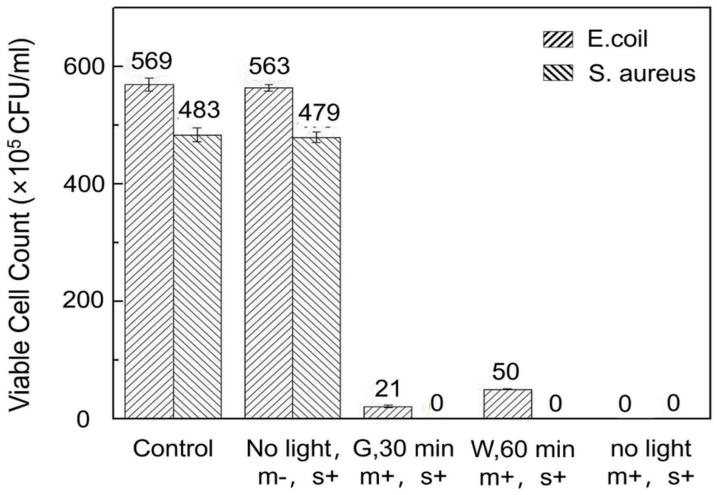

Fig. 8. Inactivation effects of the antimicrobial test specimen on *E. coli* and *S. aureus* under different conditions. G: green LED light irradiation; W: white LED light irradiation; 0: complete inactivation; m+: with Ery–DACNC–g–PTA; m-: without Ery–DACNC–g–PTA; s+: with silicone.

without any treatment, followed by 1 d of culture in an incubator. The viable count of *E. coli* in the group cultured using the pure silicone test specimen was identical to that of the control group, indicating that silicone did not affect the growth of *E. coli*. The silicone test specimen containing the antimicrobial material achieved an inactivation degree of 96.3% against *E. coli* after 30 min of green light irradiation, an inactivation degree of 91.2% against *E. coli* after 60 min of white light irradiation, and complete inactivation after 1 d of mixed culture in the absence of light.

The viable count of *S. aureus* in the group cultured with the pure silicone test specimen was also identical to that of the control group, indicating that silicone did not affect the growth of *S. aureus*. The silicone test specimen containing the antimicrobial material achieved a 100% inactivation degree against *S. aureus* after 30 min of green light irradiation, 60 min of white light irradiation, and 1 d of mixed culture in the absence of light. These results demonstrate a higher bacterial inactivation efficiency of the antimicrobial material against *S. aureus*.

3.3.3 Duration of effective microbial inactivation by 3D-printed meniscal implants

Figures 9 and 10 show the inactivation effects of the test specimens containing the antimicrobial material at weeks 4 and 7 of storage against *E. coli* and *S. aureus* after 30 min of green light irradiation. The control group was established by adding 1 mL of the bacterial solution to a sample vial without any treatment, followed by 1 d of culture in an incubator. An inactivation degree of 96.3% was achieved against *E. coli* at week 4 of storage; however, this degree dropped below the expected inactivation level of 90% by week 7. In contrast, 100% inactivation of *S. aureus* was achieved by week 7 of storage. Therefore, it can be deduced that the 3D-printed silicone/Ery–DACNC–g–PTA composite material was capable of effective bacterial inactivation after 4 weeks of storage. However, the effective service life of the material

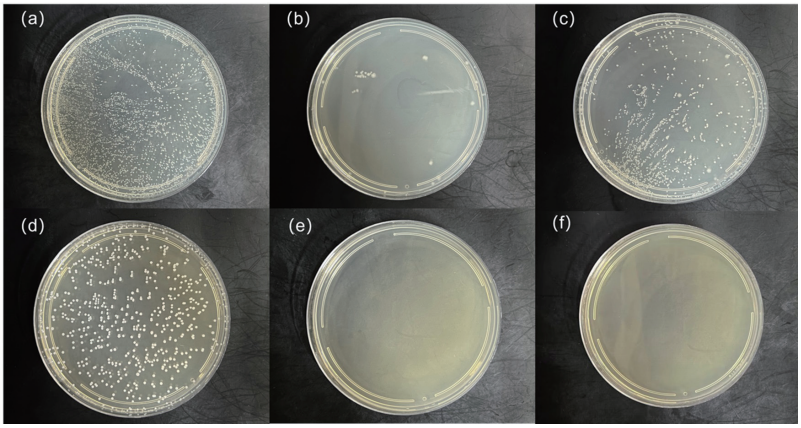

Fig. 9. (Color online) PDI effects of the test specimen at different time points on *E. coli* after 30 min of green light irradiation: (a) control group, (b) week 4 of storage, and (c) week 7 of storage. PDI effects of the test specimen at different storage time points on *S. aureus* after 30 min of green light irradiation: (d) control group, (e) week 4 of storage, and (f) week 7 of storage.

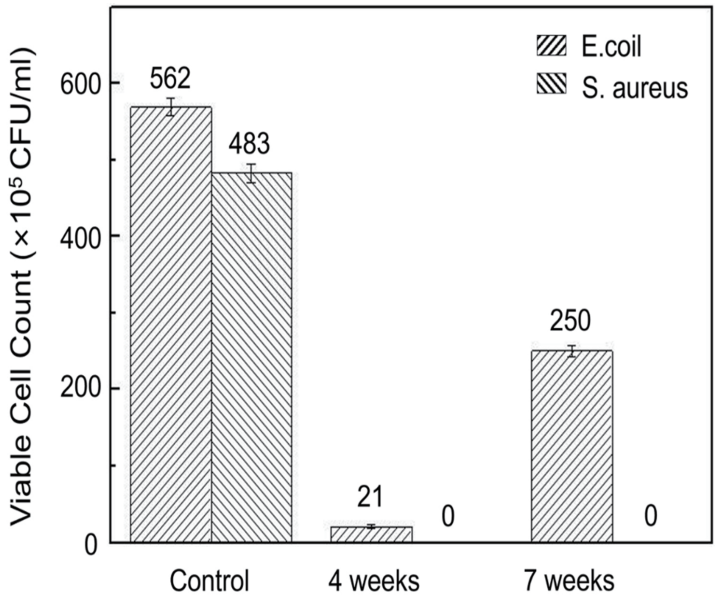

Fig. 10. Inactivation effects of *E. coli* and *S. aureus* achieved using the antimicrobial test specimen at different time points. 0: complete inactivation.

could be extended to at least 7 weeks in environments that merely required the elimination of *S. aureus*. A possible reason for this phenomenon is that the cell wall structure of *S. aureus* makes it more sensitive to PDI than *E. coli*.

3.3.4 Biocompatibility of 3D-printed meniscal implant

Figure 11 shows the viability of cells after 24 and 48 h of culture in a culture medium containing an Ery–DACNC–g–PTA silicone test specimen. The horizontal axis represents the

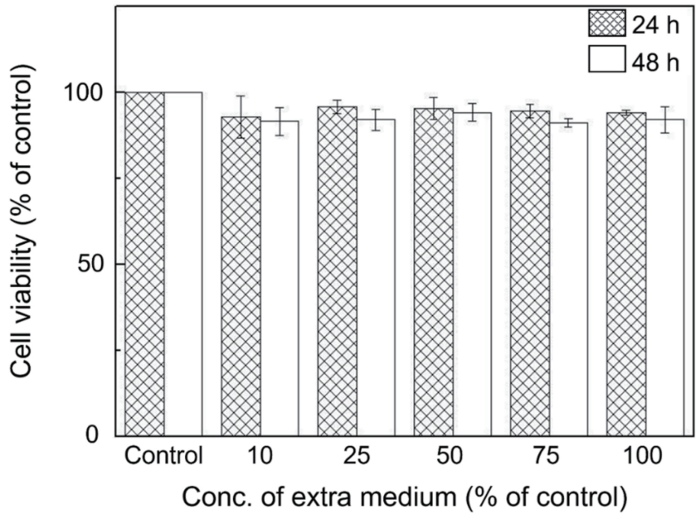

Fig. 11. Biocompatibility of silicone test specimen at 24 and 48 h using L929 cells.

volume percentage of the culture medium in the co-culture suspension containing the test specimen, and the vertical axis represents the cell viability of each experimental group relative to the control group. The control group was established using a culture medium without the test specimen. It was observed that the implants did not exhibit cytotoxicity, maintaining a cell viability of more than 90% in L929 cells after 24 and 48 h of culture, indicating the material's suitability for medical use.

4. Conclusions

In this study, we aimed to develop a green, environmentally friendly, and highly effective polymeric antimicrobial material that does not induce bacterial resistance. The prepared material was subjected to 3D printing for fabricating human meniscal implants, which are appropriate for medical applications. Our experimental results demonstrated the successful grafting of PTA onto acylated CNCs through atom transfer radical polymerization, thereby producing CNC–g–PTA. Subsequently, the aldehyde functionalization of the CNC–g–PTA was achieved using $NaIO_4$, and erythrosine was successfully grafted onto the DACNC–g–PTA using an ultrasound bath to obtain Ery–DACNC–g–PTA. Microbial inactivation experiment results showed that Ery–DACNC–g–PTA achieved the 100% inactivation of *E. coli* and *S. aureus* after 30 min of green light irradiation, 60 min of white light irradiation, or 1 d of mixed culture with bacteria in the absence of light.

The 3D-printed meniscal implant, comprising a mixture of Ery–DACNC–g–PTA and silicone, exhibited a tensile strength of 13.3 MPa, meeting the requirements for the human meniscus. Following PDI treatment with green and white light irradiations, the *E. coli* inactivation degree remained above 90%, whereas the *S. aureus* inactivation degree was 100%. Culturing the implant for 1 d without light exposure was sufficient to achieve the complete inactivation of both bacterial species. These findings indicated that the 3D-printed meniscal implant retained excellent and sustained microbial inactivation capabilities, rendering it suitable

for long-term use in real-world applications. The developed material exhibited excellent biocompatibility, an essential characteristic of materials used in the human body.

In this study, we preliminarily verified the feasibility of 3D printing technology to prepare meniscal implants with antimicrobial function. Despite these promising results, further research is needed to fully explore the sensor's capabilities and address critical aspects of the material's performance. Future studies should focus on validating the implant's mechanical properties in detail and assessing any potential local pathological effects on living tissue post-implantation. Addressing these challenges will be crucial for advancing the development of multifunctional implants that effectively combine antimicrobial and sensing capabilities for complex medical applications.

Acknowledgments

This work was supported by the National Science and Technology Council, Taiwan (grant numbers 112-2221-E-006-173, 113-2221-E-006-087-MY2, 113-2221-E-006-112-MY2, and 113-2221-E-006-116). We gratefully acknowledge the Core Facility Center of National Cheng Kung University for allowing us to use their EM000700 equipment. We also acknowledge the partial support of the Higher Education Sprout Project, Ministry of Education to the Headquarters of University Advancement at National Cheng Kung University (NCKU).

Conflict of interest

The authors declare no conflict of interest.

Credit authorship contribution statement

Conceptualization (S-CS, Y-CX)
Methodology (S-CS, Y-CX)
Sofware (Y-CX)
Validation (S-CS, C-KC, B-TK)
Format analysis (S-CS)
Investigation (Y-CX)
Resources (C-KC)
Data curation (C-KC, B-TK)
Writing: Original draft (S-CS)
Writing: draft, review, and editing (S-CS, DR)
Funding acquisition (S-CS)

References

1 M. Falcone, B. De Angelis, F. Pea, A. Scalise, S. Stefani, R. Tasinato, O. Zanetti, and L. Dalla Paola: J. Glob. Antimicrob. Resist. **26** (2021) 140. https://doi.org/10.1016/j.jgar.2021.05.010
2 S.-C. Shi, F.-I. Lu, C.-Y. Wang, Y.-T. Chen, K.-W. Tee, R.-C. Lin, H.-L. Tsai, and D. Rahmadiawan: Int. J. Biol. Macromol. **264** (2024) 130547. https://doi.org/10.1016/j.ijbiomac.2024.130547

3 E. Christaki, M. Marcou, and A. Tofarides: J. Mol. Evol. **88** (2020) 26. https://doi.org/10.1007/s00239-019-09914-3
4 R. Told, Z. Ujfalusi, A. Pentek, M. Kerenyi, K. Banfai, A. Vizi, P. Szabo, S. Melegh, J. Bovari-Biri, J. E. Pongracz, and P. Maroti: Mater. Des. **223** (2022) 111119. https://doi.org/10.1016/j.matdes.2022.111119
5 A. Rapacka-Zdończyk, A. Woźniak, K. Michalska, M. Pierański, P. Ogonowska, M. Grinholc, and J. Nakonieczna: Front. Med. **8** (2021). https://doi.org/10.3389/fmed.2021.642609
6 N. Kashef and M. R. Hamblin: Drug Resist. Updat. **31** (2017) 31. https://doi.org/10.1016/j.drup.2017.07.003
7 M. Wang, T. Wang, K. Yuan, and J. Du: Chinese J. Polym. Sci. **34** (2016) 44. https://doi.org/10.1007/s10118-016-1725-4
8 A. M. Carmona-Ribeiro and L. D. De Melo Carrasco: Int. J. Mol. Sci. **14** (2013) 9906. https://doi.org/10.3390/ijms14059906
9 H. M. Tun, R. E. Wulansari, D. Pradhan, and Z. M. Naing: J. Eng. Res. Lect. **2** (2023) 3. https://doi.org/10.58712/jerel.v2i3.103
10 Y. Singh, A. Farooq, A. Raza, M. A. Mahmood, and S. Jain: Process Saf. Environ. Prot. **111** (2017). https://doi.org/10.1016/j.psep.2017.08.041
11 H. Dong, Y. Xie, G. Zeng, L. Tang, J. Liang, Q. He, F. Zhao, Y. Zeng, and Y. Wu: Chemosphere **144** (2016). https://doi.org/10.1016/j.chemosphere.2015.10.066
12 D. Rahmadiawan, S. C. Shi, Z. Fuadi, H. Abral, N. Putra, R. Irwansyah, D. Gasni, and A. M. Fathoni: J. Tribol. **39** (2023) MYTRIBOS 2023 (Part 1).
13 D. Rahmadiawan and S.-C. Shi: Sci. Rep. **14** (2024). https://doi.org/10.1038/s41598-024-59010-w
14 C. A. Díaz-Cruz, C. Caicedo, E. J. Jiménez-Regalado, R. Díaz de León, R. López-González, R. Y. Aguirre-Loredo: Polymers **14** (2022) 2166. https://doi.org/10.3390/polym14112166
15 S.-C. Shi, C.-F. Hsieh, and D. Rahmadiawan: Teknomekanik **7** (2024) 20. https://doi.org/10.24036/teknomekanik.v7i1.30072
16 S. Van Nguyen and B. K. Lee: Carbohydr. Polym. **298** (2022) 120064. https://doi.org/10.1016/j.carbpol.2022.120064
17 M. Ikram, S. Abbas, A. Haider, S. Naz, S. O. A. Ahmad, J. Haider, A. Ul-Hamid, A. Shahzadi, I. Shahzadi, and A. R. Butt: J. Nanostructure Chem. **12** (2022) 933. https://doi.org/10.1007/s40097-021-00452-3
18 M. A. Torlopov, I. S. Martakov, V. I. Mikhaylov, K. A. Cherednichenko, and P. A. Sitnikov: Carbohydr. Polym. **319** (2023) 121169. https://doi.org/10.1016/j.carbpol.2023.121169
19 S.-C. Shi, S.-W. Ouyang, and D. Rahmadiawan: Polymers **16** (2024) 960. https://doi.org/10.3390/polym16070960
20 M. Zare, E. R. Ghomi, P. D. Venkatraman, and S. Ramakrishna: J. Appl. Polym. Sci. **138** (2021) 38. https://doi.org/10.1002/app.50969
21 T. Abdullah, R. O. Qurban, S. O. Bolarinwa, A. A. Mirza, M. Pasovic, and A. Memic: Front. Bioeng. Biotechnol. **8** (2020). https://doi.org/10.3389/fbioe.2020.568186
22 R. Nie, Y. Sun, H. Lv, M. Lu, H. Huangfu, Y. Li, Y. Zhang, D. Wang, L. Wang, and Y. Zhou: Nanoscale **14** (2022) 8112. https:/doi.org/10.1039/d2nr02176e
23 R. Gnanasambandam and A. Proctor: Food Chem. **68** (2000) 327. https://doi.org/10.1016/S0308-8146(99)00191-0
24 V. V Shevchenko, A. V. Sidorenko, V. N. Bliznyuk, I. M. Tkachenko, O. V. Shekera, N. N. Smirnov, I. A. Maslyanitsyn, V. D. Shigorin, A. V. Yakimansky, and V. V. Tsukruk: Polymer **54** (2013) 6156. https://doi.org/10.1016/j.polymer.2013.09.053
25 H. Zhang, X. Yong, J. Zhou, J. Deng, and Y. Wu: ACS Appl. Mater. Interfaces **8** (2016) 2753. https://doi.org/10.1021/acsami.5b11042
26 H.-P. Zhou, C.-H. Xu, W. Sun, and C.-H. Yan: Adv. Funct. Mater. **19** (2009) 3892. https://doi.org/10.1002/adfm.200901458